Impact of the carbon pore size and topology on the equilibrium quantum sieving of hydrogen isotopes at zero coverage and finite pressures

Impact of the carbon pore size and topology on the equilibrium quantum sieving of hydrogen isotopes at zero coverage and finite pressures

Piotr Kowalczyk[1,3]**, Piotr A Gauden**[2]**, Artur P Terzyk**[2,3,4] **and Sylwester Furmaniak**[2]

[1] Applied Physics, RMIT University, GPO Box 2476V, Victoria 3001, Australia
[2] Department of Chemistry, Physicochemistry of Carbon Materials Research Group,
Nicholas Copernicus University, Gagarin Street 7, 87-100 Torun, Poland

E-mail: E72231@ems.rmit.edu.au and aterzyk@chem.uni.torun.pl

Abstract

Carbonaceous slit-shaped and square-shaped pores efficiently differentiate adsorbed hydrogen isotopes at 77 and 33 K. Extensive path integral Monte Carlo simulations revealed that the square-shaped carbon pores enhanced the selectivity of deuterium over hydrogen in comparison to equivalent slit-shaped carbon pores at zero coverage as well as at finite pressures (i.e. quantum sieving of hydrogen isotopes is pore-topology-dependent). We show that this enhancement of the D_2/H_2 equilibrium selectivity results from larger localization of hydrogen isotopes in square-shaped pores. The operating pressures for efficient quantum sieving of hydrogen isotopes are strongly dependent on the topology as well as on the size of the carbon pores. However, for both considered carbon pore topologies the highest D_2/H_2 separation factor is observed at zero-coverage limit. Depending on carbon pore size and topology we predicted monotonic decreasing and non-monotonic shape of the D_2/H_2 equilibrium selectivity at finite pressures. For both kinds of carbonaceous pores of molecular sizes we predict high compression of hydrogen isotopes at 77 and 33 K (for example, the pore density of compressed hydrogen isotopes at 77 K and 0.25 MPa in a square-shaped carbon pore of size 2.6 Å exceeds 60 mmol cm^{-3}; for comparison, the liquid density of *para*-H_2 at 30 K and 30 MPa is 42 mmol cm^{-3}). Finally, by direct comparison of simulation results with experimental data it is explained why 'ordinary' carbonaceous materials are not efficient quantum sieves.

(Some figures in this article are in colour only in the electronic version)

1. Introduction

Understanding the separation of hydrogen isotopes by nanoporous solids, in particular carbon and zeolites, is one of the long-standing problems in adsorption and separation science. The first experimental studies on adsorption and separation of hydrogen isotopes by carbon and silica were published by Dingenen and co-workers [1], and by Hansen [2]

and Basmadjian [3, 4] between 1940 and 1960. At an early date, Russian scientists explored an application of synthetic zeolites for the separation of hydrogen isotopes near the boiling point of liquid nitrogen as well as oxygen. The fundamental experimental and theoretical studies due to Larin *et al* [5] and Polevoi and co-workers [6–9] (and references to these papers published in Russian) brought new light to the problem of quantum mixture separation by nanoporous materials. It has been shown that for any considered sample of synthetic zeolite the equilibrium selectivity at zero coverage
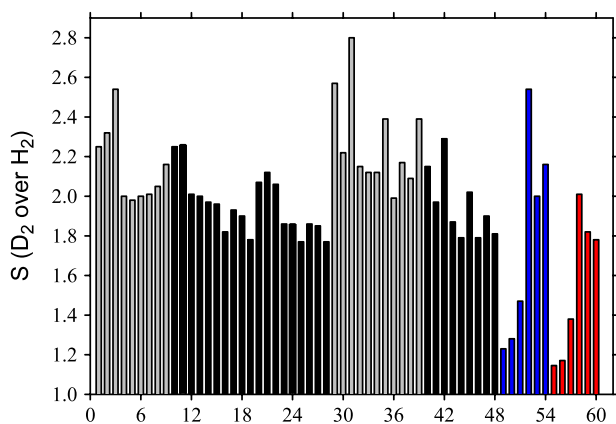
Figure 1. Experimental equilibrium selectivity of D_2 over H_2 at 77 and 90 K measured on selected samples of synthetic zeolites, silica gels and charcoals [1–9]. Abbreviations: blue bars (77 K, from left to right): Columbia 'G' charcoal, Fischer Cocoanut charcoal, silica gel, Type 4A molecular sieves, Type 5A molecular sieves and Type 13X molecular sieves; red bars (90 K, from left to right): Columbia 'G' charcoal, Fischer Cocoanut charcoal, silica gel, Type 4A molecular sieves, Type 5A molecular sieves and Type 13X molecular sieves; grey bars (77 K and various storage pressures, for details see [1–9]): NaA, MgA, CaA, ZnA, NaX, CaX and CdA; black bars (90 K and various storage pressures, for details see [1–9]): NaA, MgA, CaA, ZnA, NaX, CaX and CdA. Note that for cryogenic distillation at 20.4 K (boiling point of *para*-H_2) the D_2/H_2 separation factor is $\approx$3.0 [6].

is maximal and decreases upon the filling of the zeolite pore space. Moreover, Polevoi and co-workers estimated the change in the entropy and enthalpy of hydrogen and deuterium adsorption between 77 and 90 K [6–9]. Interestingly, the changes in the adsorption entropy for both isotopes were similar and did not depend on the temperature as well as the type of zeolite sample investigated. This explained that the efficiency of hydrogen isotopes separation is governed by the variation in the difference between the hydrogen and deuterium enthalpy of adsorption (i.e. superposition of the adsorbate–adsorbent and adsorbate–adsorbate intermolecular interactions) during the pore filling. Moreover, it has been observed that equilibrium selectivity of any investigated mixture of hydrogen isotopes reaches a maximum at zero coverage, a plateau for low pressures of separated mixtures, and further it was decreasing with the filling of zeolite pore space. For different kinds of zeolites the maximum equilibrium selectivity of deuterium over hydrogen is around 2–3 at 77 and 90 K at low surface coverage [6–9], as is presented in figure 1. However, for NaA zeolite lowering of the operating temperature to 62 K increases the D_2/H_2 separation factor up to 3.7 [6]. This is not surprising since the adsorption equilibrium selectivity of hydrogen isotopes depends exponentially on the difference in their adsorption enthalpy [10].

Recently the problem of efficient separation of hydrogen isotopes via the quantum sieving mechanism has been attracting both theorists and experimentalists. Rapid development of computers, cryogenic equipment and new methods of synthesis of nanomaterials has stimulated research in the area of nanoporous quantum filters. Tanaka *et al*

[11, 12] showed that equilibrium selectivity of D_2 over H_2 can be explained by the different quantum fluctuations of both components in the adsorbed phase. Indeed, as was shown by Beenakker *et al* [13], the higher quantum entropy of hydrogen resulting from its zero-point motion is responsible for the lowering of hydrogen content and enrichment of the deuterium amount in the adsorbed phase. Investigating the freezing of Lennard-Jones molecules in cylindrical pores Hoffmann and Nielaba [14] pointed out that the ground state oscillations destabilize the adsorbed light molecules and thus result in lower phase transition temperatures. Wang *et al* [15] and Challa *et al* [16, 17] investigated the application of an idealized model of carbon nanotube bundles for the quantum sieving of hydrogen isotopes. According to these studies, the interstitial channels formed by adjacent carbon nanotubes can be used for efficient separation of hydrogen isotopes at thermodynamic equilibrium at 20 K. Moreover, in contrast to experimental reports of hydrogen isotopes quantum sieving on zeolites, charcoals, carbon molecular sieves, silicas or single-walled carbon nanohorns, the authors predicted that the equilibrium selectivity of T_2 over H_2 or D_2 over H_2 increases during the filling of the pore space.

The goal of the work presented here is to investigate the impact of the pore size and topology of carbonaceous material on the efficiency of D_2/H_2 separation. One can argue that '*carbon is carbon*' and the investigation of the impact of carbon pore topology on the separation of hydrogen isotopes is not the fundamental issue. We show that this thesis is completely wrong since both the pore topology and size are crucial for delocalization of light molecules. In the current study we simulate equimolar mixture adsorption of deuterium and hydrogen in slit-shaped and square-shaped carbon pores at 33 and 77 K using the first-principles path integral molecular simulations. Our microscopic model assumes a spherically symmetric potential for hydrogen isotopes and realistic description of the solid–fluid interactions. As shown by Hathorn *et al* [18] as well as Garberoglio *et al* [19] our equilibrium selectivity can be regarded as a lower boundary because incorporation of the rotational degrees of freedom for hydrogen isotope molecules increases the equilibrium selectivity. The treatment of real carbonaceous material as a collection of statistically independent patches of slit-shaped or square-shaped pores is not a drastic simplification as far as we are interested in the equilibrium properties of adsorbed fluids. We compute the exact selectivity and high-temperature density matrix (i.e. wavefunction times Boltzmann factor) at zero coverage to explain an unexpected delocalization of hydrogen isotopes in selected carbonaceous pores. Next, we take into consideration the variation of equilibrium selectivity upon slit-shaped and square-shaped carbon pore loading. Here, we compare the D_2/H_2 separation factor computed from the structureless and atomistic model of graphitic pore walls. Finally, we compare our simulation results with available experimental data reported by Dingenen and van Itterbeck [1].
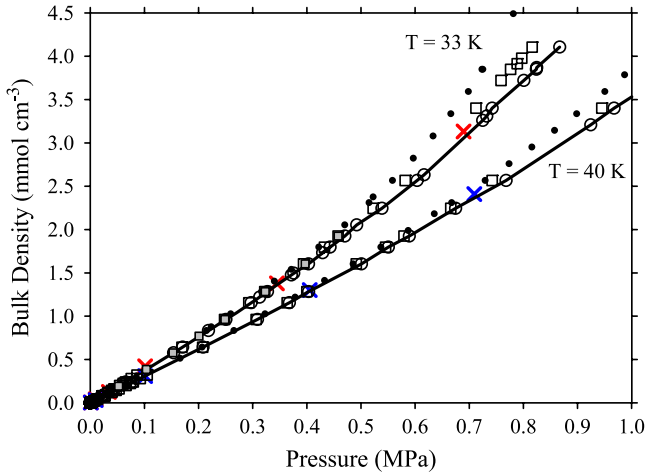
Figure 2. Pressure variation of the density of H_2 (open circles correspond to 16 beads per polymer chain) and D_2 (open squares correspond to 8 beads per polymer chain and closed grey squares correspond to 16 beads per polymer chain) at 33 and 40 K computed from PI-MC. Black circles denote classical Monte Carlo simulation and red/blue crosses show the experimental data for *para*-H_2 [38].

Figure 3. Density variation of the average kinetic energy of H_2 (open circles correspond to 16 beads per polymer chain) and D_2 (open squares correspond to 8 beads per polymer chain and closed grey squares correspond to 16 beads per polymer chain) at 33 (panel (a)) and 40 K (panel (b)) computed from PI-MC. Dashed lines denote classical kinetic energy, $K = (3/2)k_bT$.
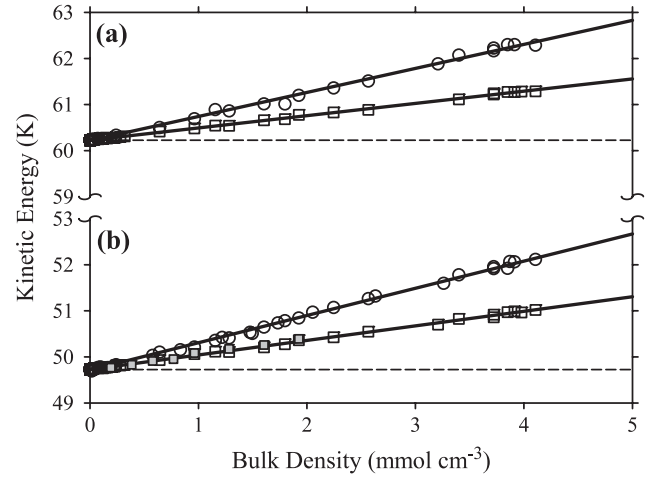
2. Simulation details

2.1. Potential models

Following Feynman's path integral formalism we used the quantum–classical isomorphism, in which each particle becomes equivalent to a chain or 'necklace' of P classical 'beads' $r_i^{(1)}, r_i^{(2)}, \ldots, r_i^{(P)}$ that accounts for the quantum delocalization of the particle [20–22]. When a system contains more than one type of quantal particle, decisions concerning the appropriative value of P should be made separately for each particle [20]. For H_2 at 33 K and moderate pressures we used $P_{H_2} = 16$ since this number of beads in a cyclic polymer reproduces the experimental equation of state, as is presented in figure 2. Since the mass of D_2 is twice the mass of H_2 the number of beads in cyclic polymers quantizing the deuterium molecule is $P_{D_2} = P_{H_2}/2 = 8$. In the considered range of experimental equations of state the mean kinetic energy of D_2 (computed for 8 and 16 beads) is within the error of simulation, as is displayed in figure 3. As previously, we quantized hydrogen and deuterium molecules at 77 K by 12 and 6 beads per cyclic polymer chain, respectively [23].

In pores, ring polymers experience both an external potential, which is the sum of the fluid–fluid and solid–fluid interactions, and an internal potential, which comes from the intermolecular bonding interactions. The effective potential can be expressed according to the so-called 'primitive action' [20–23]:

$$W = \frac{mP}{2\beta^2\hbar^2} \sum_{i=1}^{N} \sum_{\alpha=1}^{P} \left(r_i^{(\alpha)} - r_i^{(\alpha+1)} \right)^2 + \frac{1}{P} \sum_{i<j} \sum_{\alpha=1}^{P} V_{ff} \left(r_{ij}^{(\alpha)} \right)$$
$$+ \frac{1}{P} \sum_{i<j} \sum_{\alpha=1}^{P} V_{sf} \left(r_{ij}^{(\alpha)} \right) \tag{1}$$

where N is the number of atoms, $\beta = (1/k_bT)$, k_b denotes the Boltzmann constant, T is the temperature and $\hbar$ is Planck's

constant divided by 2π. Owing to the cyclic condition of the polymer chains, if $\alpha = P$, then $\alpha + 1 = 1$. For the case of the binary mixture simulation the number of beads and the mass in equation (1) depend on the type of component (here, H_2 or D_2) selected for perturbation.

Similar to Rabani *et al* [24] and Wang *et al* [15] we modelled the external interactions between the beads of ring polymers via the effective Silvera–Goldman (SG) potential [25]:

$$V_{ff}\left(r_{ij}^{(\alpha)}\right) = \exp\left(\alpha - \delta r_{ij}^{(\alpha)} - \gamma r_{ij}^{2(\alpha)}\right)$$
$$- \left(\frac{C_6}{r_{ij}^{6(\alpha)}} + \frac{C_8}{r_{ij}^{8(\alpha)}} + \frac{C_{10}}{r_{ij}^{10(\alpha)}}\right) f_C\left(r_{ij}^{(\alpha)}\right) + \frac{C_9}{r_{ij}^{9(\alpha)}} f_C\left(r_{ij}^{(\alpha)}\right) \tag{2}$$

$$f_C\left(r_{ij}^{(\alpha)}\right) = \exp\left[-\left(r_C/r_{ij}^{(\alpha)} - 1\right)^2\right] \Theta\left(r_C - r_{ij}^{(\alpha)}\right)$$
$$+ \Theta\left(r_{ij}^{(\alpha)} - r_C\right). \tag{3}$$

Here, $r_{ij}^{(\alpha)}$ is the distance between the beads labelled α of two interacting polymer chains and Θ denotes the Heaviside function. The parameters of the potential are given elsewhere [24, 25]. In nanospaces the density of adsorbed/compresses hydrogen isotopes approaches the density of a highly compressed liquid. The SG potential is a reliable representation of highly compressed hydrogen isotopes since this potential was adjusted to the solid properties of *para*-hydrogen (*ortho*-deuterium) [25].

In the current work we modelled infinitely long slit-shaped pores with a detailed atomistic arrangement of surface atoms. We adopted the Lennard-Jones potential for computation of the solid–fluid potential between the beads labelled α and surface

atoms [26]:

$$V_{sf}\left(r_i^{(\alpha)}\right) = 4\varepsilon_{sf}\left[\left(\frac{\sigma_{sf}}{r_i^{(\alpha)}}\right)^{12} - \left(\frac{\sigma_{sf}}{r_i^{(\alpha)}}\right)^{6}\right]. \quad (4)$$

Here, $r_i^{(\alpha)}$ is the distance between the selected bead of the polymer chain and surface atom. The Lorentz–Berthelot mixing rule was used for calculation of the solid–fluid potential parameters. For carbon atoms we adopted the following values of parameters: $\sigma_{C-C} = 3.4$ Å and $\varepsilon_{C-C}/k_b = 28$ K [27]. As previously, for molecular hydrogen and deuterium we used $\sigma_{ff} = 2.958$ Å and $\varepsilon_{ff}/k_b = 36.7$ K (k_b denotes Boltzmann's constant) [23, 28].

For comparative analysis we performed additional simulations adopting the structureless model of the graphitic pore wall. For this model, the external potential between an individual bead labelled α of the ring polymer and the structureless infinite planes of graphite comprising the walls of the slit-shaped pore is given by [29, 30]

$$V_{sf}\left(z_i^{(\alpha)}\right) = V_{10-4}\left(H - z_i^{(\alpha)}\right) + V_{10-4}\left(z_i^{(\alpha)}\right). \quad (5)$$

Here H denotes the width of the slit-shaped carbon pore. For the structureless graphite the solid–fluid potential depends only on the distance, z from the surface [27, 30]:

$$V_{10-4}\left(z_i^{(\alpha)}\right) = 4\varepsilon_{sf}\pi\rho_s\sigma_{sf}^2\left[\frac{1}{5}\left(\frac{\sigma_{sf}}{z_i^{(\alpha)}}\right)^{10} - \frac{1}{2}\left(\frac{\sigma_{sf}}{z_i^{(\alpha)}}\right)^{4}\right] \quad (6)$$

where $\rho_s = 0.382$ Å^{-2} is the surface density of carbon atoms in graphite and $z_i^{(\alpha)}$ is the distance of the bead labelled α of the individual ring polymer from the graphite plane.

The external potential between an individual bead labelled α of the ring polymer and the structureless infinitely long square carbon pore can be computed from [30]

$$V_{sf}\left(y_i^{(\alpha)}, z_i^{(\alpha)}\right) = \sum_{j=1}^{4}\varphi_j\left(y_j^{(\alpha)}, z_j^{(\alpha)}\right) \quad (7)$$

where $\varphi(y, z)$ denotes the external solid–fluid interaction potential between the selected bead labelled α of the ring polymer and the finite structureless carbon strip of length $2L$ [30]:

$$\varphi(y, z) = \frac{252}{256}\varepsilon_{sf}\sigma_{sf}^{12}\rho_s\pi\zeta_1(y, z) - \frac{3}{2}\varepsilon_{sf}\sigma_{sf}^6\rho_s\pi\zeta_2(y, z) \quad (8)$$

where

$$\zeta_1(y, z)$$
$$= \frac{1}{315}\left\{\frac{b\left(840z^6b^2 + 315z^8 + 1008z^4b^4 + 576z^2b^6 + 128b^8\right)}{z^{10}\left(b^2 + z^2\right)^{9/2}}\right.$$
$$\left. - \frac{a\left(840z^6a^2 + 315z^8 + 1008z^4a^4 + 576z^2a^6 + 128a^8\right)}{z^{10}\left(a^2 + z^2\right)^{9/2}}\right\}$$
$$(9)$$

$$\zeta_2(y, z) = \frac{1}{3}\left\{\frac{b\left(3z^2 + 2b^2\right)}{z^4\left(b^2 + z^2\right)^{3/2}} - \frac{a\left(3z^2 + 2a^2\right)}{Z^4\left(a^2 + z^2\right)^{3/2}}\right\}. \quad (10)$$

Here $a = -L - y$ and $b = L - y$. The assumption of the structureless form of the flat surface is realistic for high temperatures (>77 K) due to the high thermal energy of the quantum particles. In other words, the oscillations of the sold–fluid potential generated by the graphite wall are smoothed out. Nevertheless, this simplified model of the solid–fluid interactions is a reasonable approximation for adsorption of hydrogen isotopes at cryogenic temperatures.

2.2. Path integral Monte Carlo simulation of H_2 and D_2 in the grand canonical ensemble

Single-component isotherms of H_2 and D_2 adsorbed in the slit-shaped and square-shaped carbon pores were simulated in the Grand Canonical ensemble (i.e. fixed system volume V, temperature T and chemical potential μ_p) [31]. We adopted three types of moves in our path integral GCMC simulations: particle displacement, creation and deletion [31]. The displacement step was realized by two independent algorithms. The first displacement perturbation is a classical 'bead-per-bead' sampling with an additional movement of the whole selected cyclic path according to the displacement of the centroid [32–34]. The probability of accepting a trial displacement move is given by the standard Metropolis sampling scheme [31]:

$$acc\left(s \rightarrow s'\right) = \min\left\{1, \exp\left(-\beta\Delta U\right)\right\} \quad (11)$$

where $\Delta U = U(r'^N) - U(r^N)$ is the change in the total energy of the simulation system and $\beta = (k_bT)^{-1}$. Displacement step size has been adjusted to give an acceptance ratio of 50%. It is well known that this primitive sampling is very inefficient. To overcome this sampling problem we propose to sample the configuration of H_2 and D_2 adsorbed in carbon pores according to the 'bisection' method [32–34]. The details of bisection sampling are given elsewhere [34]. The trial insertion/deletion of particles was performed according to the Wang *et al* [15] description. To maintain microscopic reversibility we set up equal probabilities for trial displacement, creation and destruction of a selected particle. The chemical potential of deuterium/hydrogen calculated in the canonical ensemble was used as an input in PI-GCMC simulations. The bead–bead intermolecular cutoff distance was $5\sigma_{ff}$. We did not add the long-range corrections because the fluid in the pores is inhomogeneous and the potential energy rapidly approaches zero beyond the $5\sigma_{ff}$ limit. Simulation runs were performed at gradually increasing chemical potentials, and the resulting configurations from one condition were used to initiate the subsequent calculations at higher chemical potentials. The grand canonical ensemble simulations utilized 2×10^8 configurations, of which the first 1×10^8 were discarded to guarantee equilibration. The stability of the results was confirmed by additional longer runs of 3×10^8 configurations, with the equilibrium averages for hydrogen in pores fully reproducible. For each point on the simulated isotherm we performed three independent PI-GCMC runs to average the final equilibrium averages. We used the same simulation set-up for the case of H_2/D_2 equimolar mixture adsorption in the slit-shaped and square-shaped carbon pores. The component of the binary mixture for displacement, insertion and deletion perturbation was selected with equal probability.

2.3. High-temperature density matrix

Path integral simulation can be directly used for measurement of the high-temperature density matrix, i.e. wavefunction times Boltzmann factor [20, 21]. Let us consider one quantum particle immersed in a one-dimensional external potential $V(x)$. The effective potential can be expressed according to the so-called 'primitive action' [20, 21]:

$$W\left(x^1, x^2, \ldots, x^P\right) = \frac{mP}{2\beta^2\hbar^2} \sum_{\alpha=1}^{P} \left(x^{(\alpha)} - x^{(\alpha+1)}\right)^2$$
$$+ \frac{1}{P} \sum_{\alpha=1}^{P} V(x^{(\alpha)}) \qquad (12)$$

owing to the cyclic condition of the polymer chains, where $x^{P+1} = x^1$. During the stochastic Monte Carlo process we generate the sequence of equilibrium states ζ_l, $l = 1, 2, \ldots$. The efficient method used for evaluation of the high-temperature density matrix from $\{\zeta_l\}$ is as follows. We divide the real space x into a large number of bins $[m\Delta, (m+1)\Delta)m = 0, 1, 2, \ldots$. After initial equilibration of the system, we monitored sequences of $\{\zeta_l\}$ generated from the stochastic Monte Carlo process. The jth component of ζ_l falls into some bin $[m\Delta, (m+1)\Delta)$. A point $x^j \in \zeta_l$, $j = 1, 2, \ldots, P$ is stored for that bin. As the stochastic Monte Carlo process continues, each bin accumulates points (i.e. path coordinates) with each successful entry or persistence in that bin. The high-temperature density matrix is then proportional to the total number of points in the bin. The extension of equation (12) for the two-and three-dimensional potential $V(r)$ is obvious.

2.4. Equilibrium selectivity of deuterium over hydrogen at zero and finite pressures

In the zero-pressure limit, the equilibrium selectivity of D_2/H_2 can be directly calculated from the path integral Monte Carlo simulation as a ratio between the partition function of D_2 over H_2 [15, 27]:

$$S_0(p=0) = \frac{\int d\Gamma \int d\omega \int dr \exp\left[-U_{D_2}(\Gamma, \omega, r)/k_bT\right]}{\int d\Gamma \int d\omega \int dr \exp\left[-U_{H_2}(\Gamma, \omega, r)/k_bT\right]} \qquad (13)$$

where U denotes the configurational energy, r is the position of the ring centre of mass, and Γ and ω are the path's internal conformation and orientation in the pore, respectively. In the current paper, we computed zero-pressure selectivity from equation (13) using the method proposed by Wang *et al* [15]. At finite pressure, equilibrium selectivity of D_2 over H_2 represents the ratio of the density of these two species in a porous material to the ratio of the density in the bulk phase [27, 35]:

$$S = \frac{\rho_{D_2}^p / \rho_{H_2}^p}{\rho_{D_2}^b / \rho_{H_2}^b} \qquad (14)$$

where ρ_i^p and ρ_i^b are the average densities of species i in the tube and bulk phase, respectively. A value greater than unity implies that D_2 is preferentially adsorbed compared to H_2; in contrast, if the selectivity is smaller than unity,

H_2 is preferentially adsorbed. We computed equilibrium selectivity of D_2 over H_2 at finite pressures from PI-GCMC and equation (14).

2.5. Pore density of hydrogen and deuterium

The absolute value of the binary mixture, hydrogen and deuterium component adsorption (i.e. density of the mixture and each component in the pore), is simply given by [35, 36]

$$\Gamma = \frac{\langle N_{H_2} + N_{D_2} \rangle}{V}, \qquad \Gamma_{H_2} = \frac{\langle N_{H_2} \rangle}{V}, \qquad \Gamma_{D_2} = \frac{\langle N_{D_2} \rangle}{V} \qquad (15)$$

where $\langle \cdots \rangle$ denotes the ensemble average number of hydrogen/deuterium molecules in the volume of the simulation box. For infinitely long slit-shaped carbon pores the accessible volume of the pore is $V = L_x L_y (L_z - \sigma_{ss})$, whereas for infinitely long square-shaped carbon pores $V = (L_x - \sigma_{ss})(L_y - \sigma_{ss})L_z$, where $\sigma_{ss} = 3.4$ Å.

2.6. Enthalpy of adsorption per mole

The enthalpy of adsorption per mole for adsorption of a single quantum particle can be computed from the fluctuation theorem [23, 26, 36]:

$$Q = \frac{5}{2}k_bT - \frac{3}{2}Pk_bT - \frac{\langle W_2 N \rangle - \langle W_2 \rangle \langle N \rangle}{\langle N^2 \rangle - \langle N \rangle^2}$$
$$- \frac{\langle W_1 \rangle \langle N \rangle - \langle W_1 N \rangle}{\langle N^2 \rangle - \langle N \rangle^2} \qquad (16)$$

where

$$W_1 = \frac{mP}{2\beta^2\hbar^2} \sum_{i=1}^{N} \sum_{\alpha=1}^{P} \left(r_i^{(\alpha)} - r_i^{(\alpha+1)}\right)^2 \qquad (17)$$

$$W_2 = \frac{1}{P} \sum_{i<j} \sum_{\alpha=1}^{P} V_{ff}\left(r_{ij}^{(\alpha)}\right) + \frac{1}{P} \sum_{i<j} \sum_{\alpha=1}^{P} V_{sf}\left(r_{ij}^{(\alpha)}\right). \qquad (18)$$

In the above $\langle \cdots \rangle$ is the ensemble average computed from PI-GCMC and N denotes the number of quantum particles. Due to quantum fluctuations equation (16) contains a correction to the classical kinetic energy, which is known as the thermodynamics estimator [34, 37]:

$$K = \frac{3}{2}NPk_bT - \frac{mP}{2\beta^2\hbar^2} \sum_{i=1}^{N} \sum_{\alpha=1}^{P} \left(r_i^{(\alpha)} - r_i^{(\alpha+1)}\right)^2. \qquad (19)$$

In the classical limit, that is for $P = 1$, equation (16) is reduced to [26]

$$Q = k_bT - \frac{\langle W_2 N \rangle - \langle W_2 \rangle \langle N \rangle}{\langle N^2 \rangle - \langle N \rangle^2}.$$

Note that for $P = 1$ all fluctuations in imaginary time vanish and the kinetic energy is equal to $(3/2)k_bT$. The extension of equation (16) to a quantum mixture adsorption is obvious.

3. Results and discussion

3.1. Equation of state

Before discussing the various aspects related to the H_2/D_2 equimolar mixture adsorption in slit-shaped and square-shaped carbon pores, let us focus on the reproduction of the experimental equation of state (EOS) at 33 and 40 K and pressures up to 1 MPa by the path integral method implemented in a canonical ensemble (PI-MC) [38]. At very low densities, the mean kinetic energy values of both H_2 and D_2 estimated by our PI-MC simulations approach the classical limit, i.e. $K \rightarrow (3/2)k_bT$. However, at pressures over 0.5 MPa we observe a deviation of the classical EOS from the experimental data [38]. If quantum effects are neglected a strong attraction between *para*-H_2 molecules appears that artificially enhances the density of this quantum fluid, as is shown in figure 2. A linear increase in the mean kinetic energy with the density of both H_2 and D_2 is observed, as displayed in figure 3. This linear dependence is derived from the low-density range of quantum fluids studied here. However, we can expect highly nonlinear variation of the mean kinetic energy in a dense *para*-H_2/*ortho*-D_2 because of the confining effects of the hard cores (i.e. the quantum particle is confined by the hard cores generated from the nearest-neighbour molecules that increase its kinetic energy).

3.2. High-temperature density matrix

The impact of the carbonaceous pore topology as well as its size on the localization of hydrogen isotopes at 33 K is displayed in figures 4 and 5. At first, we found that for both the slit-shaped and square-shaped carbon pores the lighter hydrogen isotopes are more delocalized than the heavier ones. This effect is obvious and can be attributed to the higher quantum entropy of lighter hydrogen isotopes (i.e. higher zero-point motion of hydrogen molecules than deuterium or tritium molecules). In the smallest slit-shaped/square-shaped carbon pores adsorbed hydrogen isotopes are exposed to enormous solid–fluid interaction potentials characterized by the steep single minima. Under the strong confinement, D_2 molecules tend to be localized at the centre of the pore, as is shown in figures 4 and 5. As expected, for H_2 molecules, higher fluctuations in imaginary time cause broadening of the high-temperature density matrix, as is displayed in figures 4 and 5. Moreover, regardless of the topology of the carbon pore, we observe a high similarity between the H_2 and D_2 high-temperature density matrix near the carbon pore widths of 4.3–4.4 Å, as is shown in figures 4 and 5. In those slit-shaped (as well as square-shaped) carbon pores the solid–fluid potential minima generated from the opposed carbon pore walls merge inside the pore. This simply means that adsorbed quantum paths have a space for their delocalization and they are not affected by confinement. The slit-shaped/square-shaped carbon pores of pore widths of 4.3–4.4 Å can be treated as virtual pores. Further extension of the pore size affects the high-temperature density matrix of hydrogen isotopes due to creation of the potential barrier in the middle of the pore, as is displayed in figures 4 and 5. As for the smallest carbon pores,
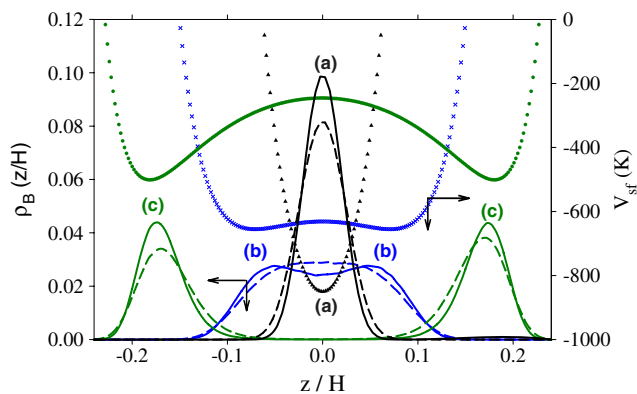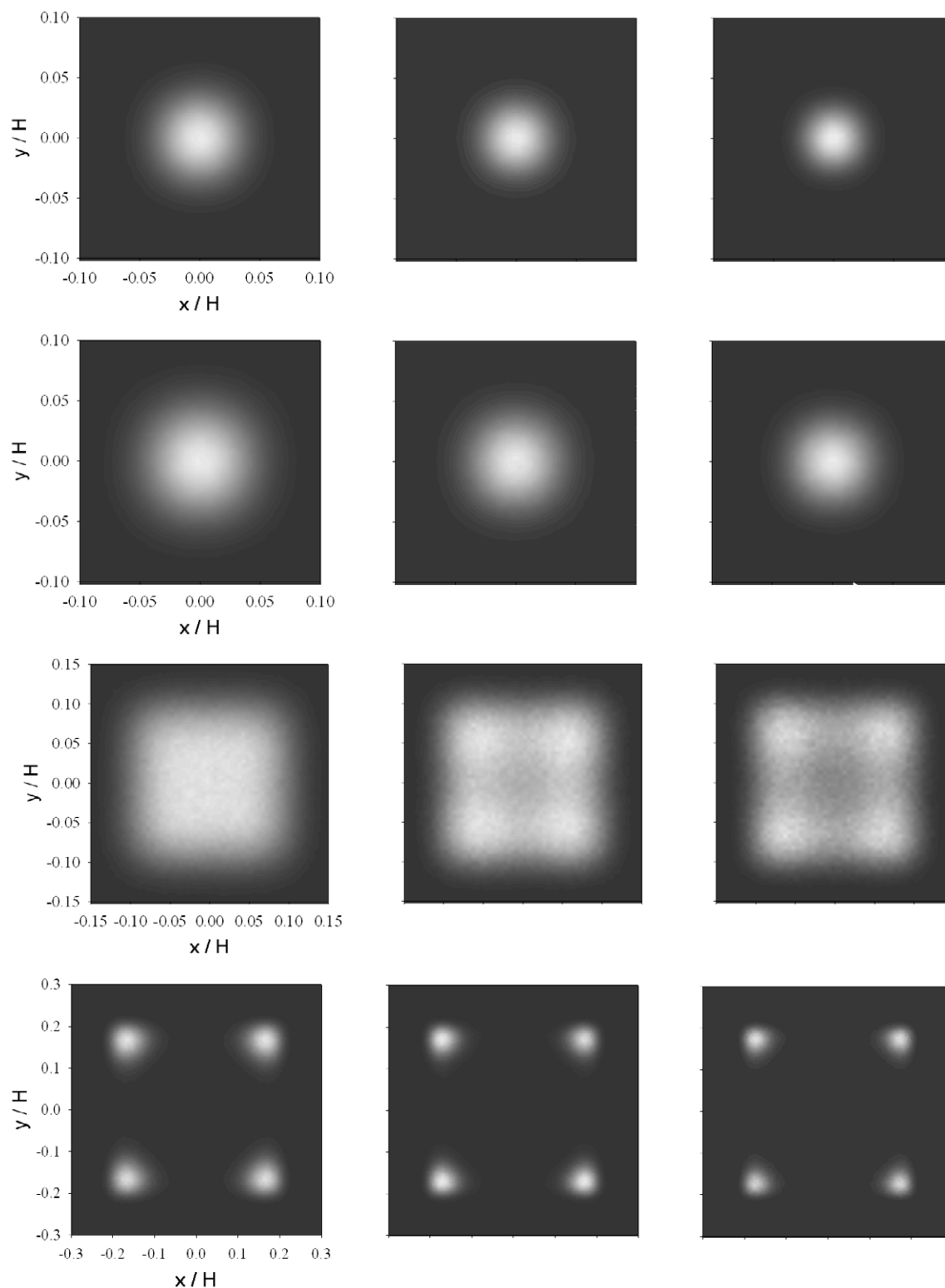

Figure 4. High-temperature density matrix (left ordinate) of D_2 (solid lines) and H_2 (dashed lines) at 33 K and zero coverage computed for infinity-long structureless slit-shaped carbon pores of pore width: (a) 2.6 (black), (b) 4.3 (blue) and (c) 6.6 Å (green). The solid–fluid potential (points) is labelled on the left ordinate.

D_2 molecules tend to be localized near the pore walls where the quantum polymer chains fluctuate in the solid–fluid minimum well depths. As expected, higher zero-point motion of H_2 molecules causes broadening of its high-temperature density matrix, i.e. due to the higher excess of the kinetic energy H_2 molecules can penetrate the regions of the solid–fluid potential that are inaccessible for the classical molecules.

Note that square-shaped carbon pores localize hydrogen isotopes more strongly than equivalent slit-shaped carbon pores, as is presented in figures 4 and 5. As we will show later this quantum phenomenon directly impacts the equilibrium D_2/H_2 selectivity at zero and finite pressures.

3.3. Equilibrium selectivity of D_2 over H_2 at zero coverage

We start discussing the equilibrium selectivity of D_2 over H_2 in slit-shaped and square-shaped carbon pores computed at zero coverage. The key point is that, regardless of the operating temperature, the square topology of the carbon pores enhanced the equilibrium selectivity of D_2 over H_2 in comparison to ordinary slit-shaped carbon pores. The fluctuating quantum paths are exposed to stronger solid–fluid potentials inside the square-shaped carbon pores than inside the equivalent slit-shaped carbon pores. Higher differences between the quantized energy levels of H_2 and D_2 adsorbed in a square-pore topology enhanced D_2/H_2 equilibrium selectivity, as is presented in figures 6 and 7. Moreover, regardless of the topology of the carbon pore, we observe the deep minima of the D_2/H_2 equilibrium selectivity near the pore widths of 4.3–4.4 Å, as is shown in figures 6 and 7. As we mentioned above, this purely quantum phenomenon is caused by the flat shape of the solid–fluid potential inside these carbon pores. This simply means that the solid–fluid potential inside these particular pores does not break the symmetry of fluctuating H_2 and D_2 polymer chains. Consequently, the D_2/H_2 equilibrium selectivity is drastically reduced, since the confined quantum hydrogen isotopes behave as their bulk counterparts. Note that this quantum phenomenon does not depend on the carbon pore topology, i.e. the carbonaceous pores of pore widths

Figure 5. High-temperature density matrix of H_2 (left panel), D_2 (middle panel) and T_2 (right panel) adsorbed in infinitely long structureless square-shaped carbon pores of widths: 2.6, 3.1, 4.4 and 6.6 Å (from top to bottom).

around 4.3–4.4 Å can be treated as virtual pores. Further extension of the slit-shaped as well as square-shaped pore sizes increases equilibrium selectivity due to the creation of the potential barrier in the middle of the pore, as is shown in figures 4–8. Due to the higher potential barrier, square-shaped pores enhanced the D_2/H_2 equilibrium separation factor in comparison to the equivalent slit-shaped graphite pores (figures 6 and 7). The variation of the kinetic energy of
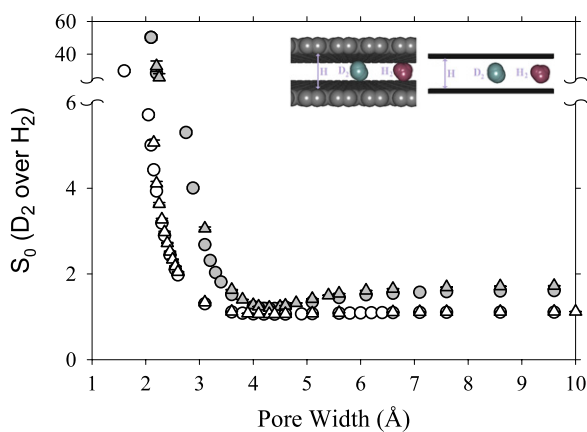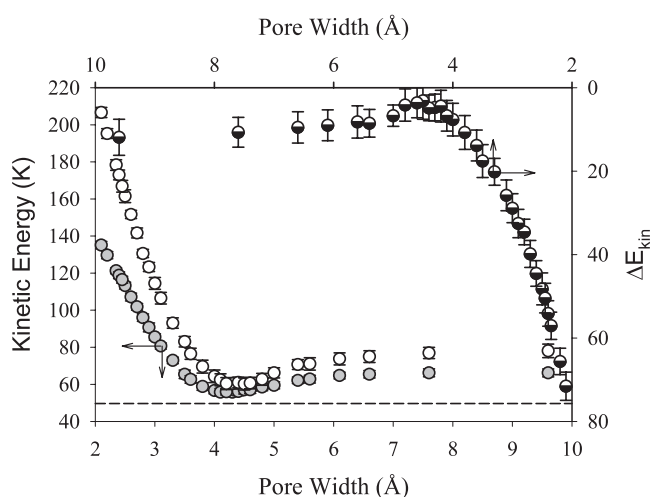
Figure 6. Equilibrium selectivity of D_2 over H_2 (computed at zero coverage) as a function of infinitely long slit-shaped carbon pore widths: white symbols—77 K, grey symbols—33 K. Abbreviations: circles—structureless and triangles—atomistic slit-shaped graphitic carbon pores.
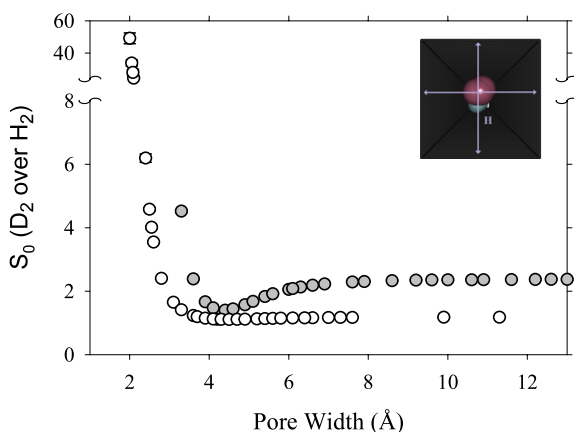
Figure 7. Equilibrium selectivity of D_2 over H_2 (computed at zero coverage) as a function of infinitely long square-shaped structureless carbon pore widths: white symbols—77 K, grey symbols—33 K.

Figure 8. Kinetic energy of H_2 (white circles) and D_2 (grey circles) (computed at 33 K and zero coverage) versus infinitely long structureless slit-shaped carbon pore widths. Right plot presents the difference between the kinetic energy of both hydrogen isotopes. The parallel dashed line denotes the classical kinetic energy at 33 K, i.e. $K = (3/2)k_bT$.

H_2 and D_2 at 33 K and zero coverage upon the size of the structureless slit-shaped carbon pores is presented in figure 8. As a consequence of Heisenberg's uncertainty principle, in the smallest carbon pores the kinetic energy of both hydrogen isotopes can reach very high values (figure 8). What is more important, the smaller the size of the carbon pore is, the higher is the difference between the kinetic energy of H_2 and D_2. That is why the reduction in the carbon pore size increases the D_2/H_2 equilibrium separation factor (figures 6 and 7).

Summing up, for both slit-shaped and square-shaped carbon pore topology the steepness of the solid–fluid potential (and not the size of the pore) is a key parameter governing the efficiency of hydrogen isotope separation. This steepness of the solid–fluid potential is responsible for high localization and the enhancement of the average kinetic energy of the hydrogen isotopes. Our results displayed in figures 4–8 explain recent experimental reports of the higher kinetic energy of confined quantum particles in comparison to the bulk ones [39, 40]. Kinetic energy in quantum mechanics

is a curvature of the wavefunction at zero temperature. Our simulations show that the strong and steep solid–fluid potential reduced the delocalization of hydrogen isotopes (i.e. increased the curvature of the high-temperature density matrix, as is presented in figures 4 and 5). The smaller the size of the carbon pores is, the more localized is the state of the confined quantum particle. Finally, the efficiency of quantum sieving of hydrogen isotopes by carbonaceous materials strongly depends on the topology of the pores. This observation seems to be particularly important for designing an efficient molecular sieve for cryogenic separation of hydrogen isotopes via the quantum sieving mechanism.
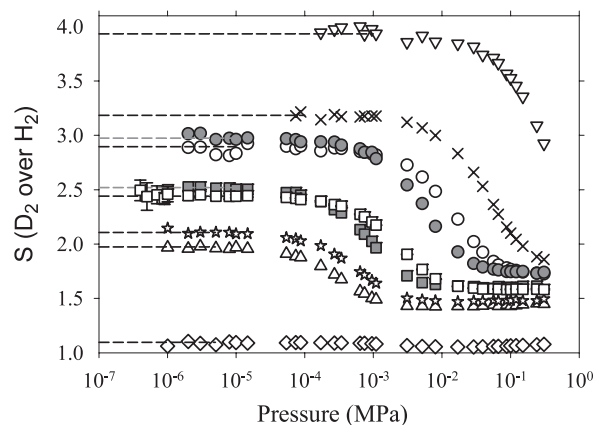
3.4. Pore density, enthalpy of adsorption and equilibrium selectivity of D_2 over H_2 at finite pressures

It is important to note that many separation processes of industrial importance occur at nonzero loading. Relative to the infinite dilution case, the addition of molecules to carbon pores leads to additional fluid–fluid interactions, inevitably affecting the variation of the D_2/H_2 equilibrium factor at finite pressures. The experimental results of D_2/H_2 mixture separation in zeolites, charcoals, carbon molecular sieves and silicas showed that D_2/H_2 equilibrium selectivity is lowered upon increasing of the operating temperature as well as the pressure of the mixture (see [1–9]). The exponential reduction of the D_2/H_2 equilibrium selectivity during increases in the operating temperature can be easily explained by the fact that all quantum fluctuations in imaginary time vanish at high temperatures. Simply, at sufficiently high temperatures H_2 and D_2 molecules behave as classical particles. However, the question of why the D_2/H_2 equilibrium selectivity is reduced upon increasing the mixture's pressure at fixed temperature is nontrivial. Moreover, path integral Monte Carlo simulations due to Challa *et al* [16, 17] predicted that
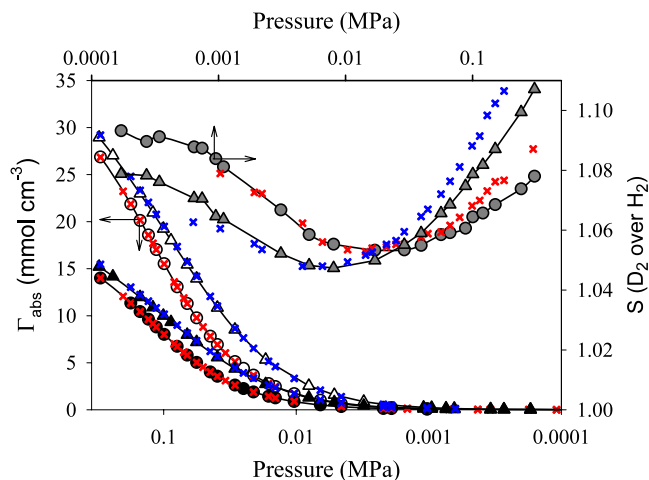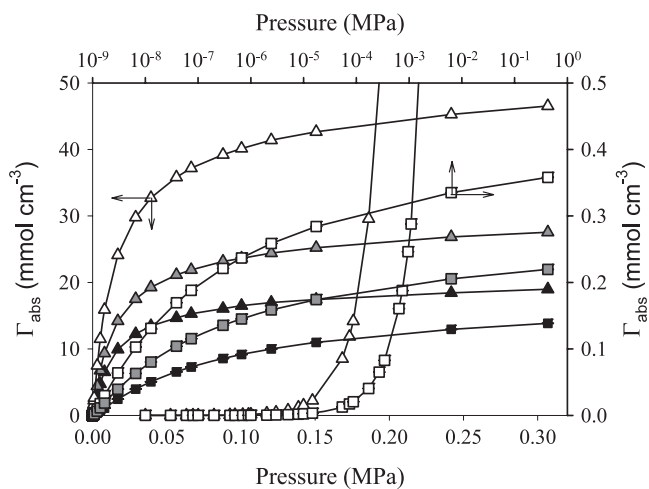
Figure 9. Pressure variation of the D_2 and H_2 pore density as well as D_2/H_2 equilibrium selectivity computed for an equimolar mixture of D_2/H_2 adsorbed in infinitely long structureless slit-shaped carbon pores (at 77 K) of widths 5.6 (triangles) and 6.6 Å (circles). Abbreviations: circles and triangles denote PI-GCMC simulations and crosses were computed from an effective second-order Feynman–Hibbs potential [29, 30].

Figure 10. Equilibrium selectivity of D_2 over H_2 at 77 K for various widths of infinitely long slit-shaped carbon pores: 2.2 (triangles down), 2.3 (crosses), 2.35 (circles), 2.45 (squares), 2.55 (stars), 2.6 (triangles up) and 6.6 Å (diamonds) computed from PI-GCMC. All filled grey symbols correspond to a structureless model of the carbon pore walls and open symbols correspond to the atomistic graphitic pore walls. Dashed lines denote calculations at zero coverage.

the equilibrium selectivity of T_2 over H_2 or D_2 over H_2 is increasing during the filling of the single-walled nanotubes as well as interstitial channels between the nanotubes forming a hexagonal bundle assembly. Careful analysis of the current simulation results revealed that D_2/H_2 equilibrium selectivity can be either an increasing or decreasing function of the pore loading (i.e. mixture pressure), as is shown in figures 9, 10 and 13. We found that for wider slit-shaped carbon pores the D_2/H_2 equilibrium separation factor at 77 K is a non-monotonic function of the pore loading (figure 9). Here, we observed initial decreasing and further increasing in the D_2/H_2 equilibrium selectivity. Note that two independent simulation techniques predict the same variation of the D_2/H_2 mixture separation with mixture pressure. At low D_2/H_2 equimolar mixture pressures the total intermolecular potential being the sum of the solid–fluid and fluid–fluid interactions is governed by the shape of the solid–fluid potential. In wider slit-shaped carbon pores the solid–fluid potential can be represented by the classical symmetric double-well potential (i.e. there is a potential barrier at the centre of the carbon pore). During the filling of the carbon pore space the fluid–fluid interactions between adsorbed hydrogen isotopes effectively lower this barrier. Since the topology of the total effective potential is changed, the D_2/H_2 equilibrium separation factor is a non-monotonic function of the mixture pressure. For the smallest slit-shaped as well as square-shaped carbon pores we observed a monotonic decrease in the D_2/H_2 equilibrium selectivity upon increasing the mixture pressure (figures 10 and 13). In contrast to wider carbon pores, the solid–fluid potential in these carbon pores can be represented by the symmetric single-well potential. During the filling of these carbon pores the fluid–fluid interactions reduce the effective interactions with carbon pore walls but do not change the topology of the total effective potential. This explains the monotonic variation in the D_2/H_2 selectivity upon pore loading.
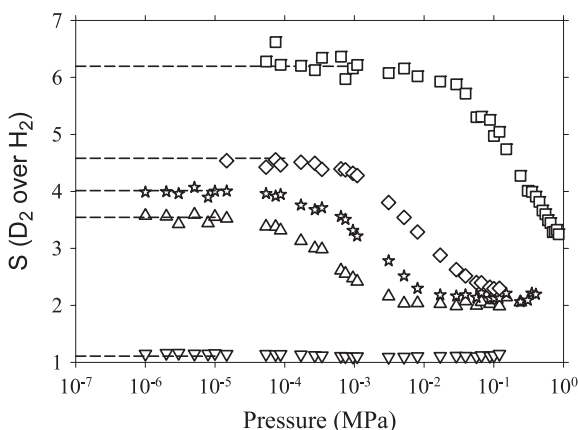

Figure 11. Pressure variation of adsorbed density of the D_2/H_2 mixture (open symbols), D_2 mixture component (grey symbols) and H_2 mixture component (black symbols) at 77 K. The presented PI-GCMC simulation results correspond to infinitely long structureless slit-shaped carbon pore sizes of 2.45 (squares) and 2.6 Å (triangles).

It is interesting to compare the properties of confined hydrogen isotopes with their bulk counterparts. Both slit-shaped and square-shaped carbon pores highly compress hydrogen isotopes (figures 11 and 14). The liquid density of *para*-H_2 at 30 K and 1 MPa is 28 mmol cm^{-3} (for 30 MPa it is 42 mmol cm^{-3}). The density of the compressed hydrogen isotopes at 77 K and 0.25 MPa in square-shaped carbon pores of size 2.6 Å exceeds 60 mmol cm^{-3}. The high compression of the adsorbed hydrogen isotopes results from the enormous solid–fluid potential in these pores. As one can expect, the square topology of the carbon pores enhanced the density of the adsorbed hydrogen isotopes in comparison to the equivalent slit-shaped carbon pores due to overlapping of the solid–fluid potential generated from the four carbon pore walls. Carbon
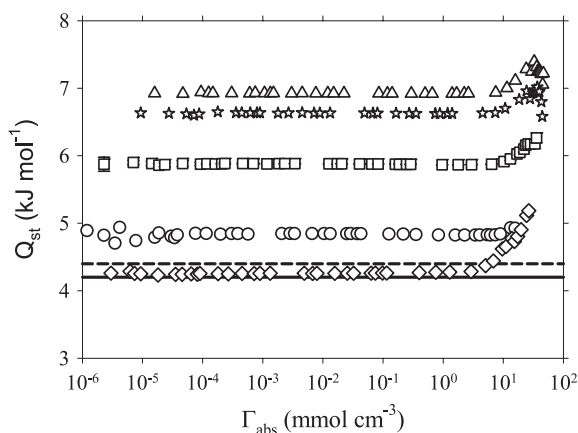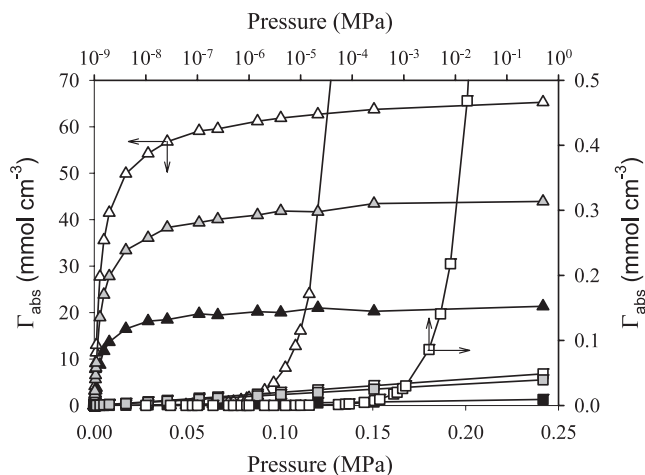
Figure 12. Pore density variation of the enthalpy of adsorption at 77 K for various widths of infinitely long structureless slit-shaped carbon pores: 2.35 (circles), 2.45 (squares), 2.55 (stars), 2.6 (up triangles) and 6.6 Å (diamonds) computed from PI-GCMC. For comparison purposes the experimental enthalpy of adsorption of H_2 (dashed line) and D_2 (solid line) on graphite is included.

Figure 14. Pressure variation of adsorbed density of the D_2/H_2 mixture (open symbols), D_2 mixture component (grey symbols) and H_2 mixture component (black symbols) at 77 K. The presented PI-GCMC simulation results correspond to infinitely long structureless square-shaped carbon pore sizes of 2.4 (squares) and 2.6 Å (triangles).
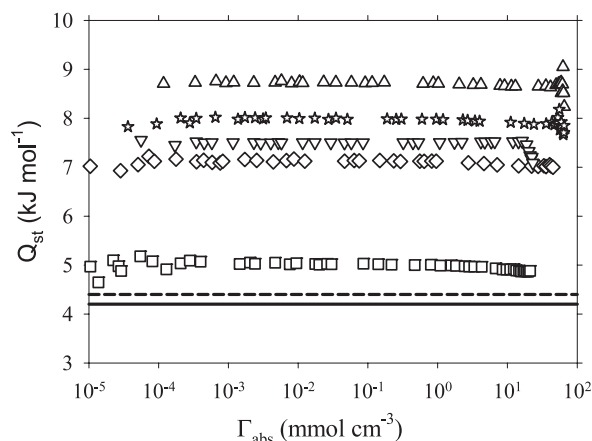

Figure 13. Equilibrium selectivity of D_2 over H_2 for various widths of infinitely long square-shaped carbon pores: 2.4 (squares), 2.5 (diamonds), 2.55 (stars), 2.6 (up triangle) and 4.6 Å (down triangle) computed from PI-GCMC. All symbols correspond to a structureless model of the carbon pore walls. Dashed lines denote calculations at zero coverage.

Figure 15. Pore density variation of enthalpy of adsorption at 77 K for various widths of infinitely long structureless square-shaped carbon pores: 2.4 (squares), 2.5 (diamonds), 2.55 (stars), 2.6 (up triangle) and 4.6 Å (down triangle) computed from PI-GCMC. For comparison purposes the experimental enthalpy of adsorption of H_2 (dashed line) and D_2 (solid line) on graphite is included.

pore topology and size impact on the enthalpy of adsorption of hydrogen isotopes due to the different packing of confined molecules (figures 12 and 15). The enthalpy released during the adsorption of an equimolar mixture of D_2/H_2 at 77 K in slit-shaped pores of size 2.6 Å (i.e. perfect pores that accommodate one layer of adsorbed molecules) is around 7 kJ mol^{-1}. Moreover, square-shaped carbon pores of the same size enhanced the enthalpy of adsorption up to 8.7 kJ mol^{-1}. Note that for the smallest slit-shaped as well as square-shaped carbon pores both the density and the enthalpy of adsorption of hydrogen isotopes at 77 K are reduced due to the action of the repulsive potential between the opposite carbon pore walls. On the other hand, extending the slit-shaped or square-shaped carbon pore sizes above ≈2.6 Å drastically reduces the density and enthalpy of hydrogen isotopes at 77 K since the confinement effect is reduced to that corresponding to an open graphite surface.

It would be instructive to compare our simulation results with available experimental data [1]. It is documented that the slit-shaped carbon pore model successfully explained the equilibrium properties of classical as well as quantum molecules adsorbed in activated carbon, activated carbon fibres and charcoals [29]. Our PI-GCMC simulation results quantitatively reproduce the experimental ratio between the density of D_2 and H_2 adsorbed in charcoal at 77 and 33 K reported by Dingenen and van Itterbeck [1] (figures 16 and 17). Moreover, our theoretical results explain why the current carbonaceous materials are not efficient quantum sieves at 77 or 33 K. The average width of the slit-shaped carbon pores of charcoal is around 5.6 Å. Clearly, this pore size is too wide for efficient sieving of hydrogen isotopes at 77 or 33 K
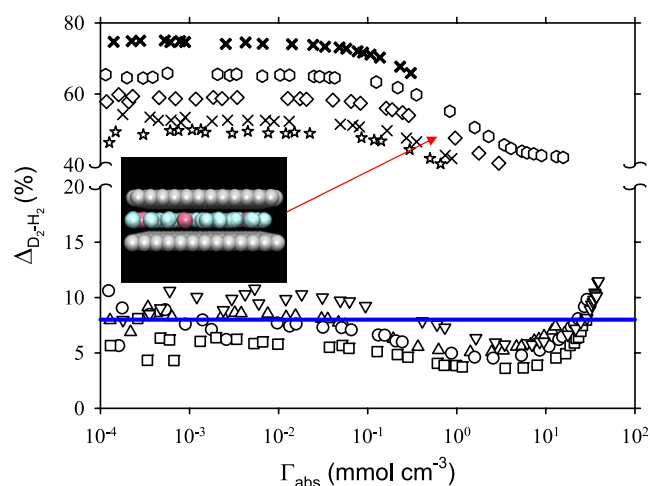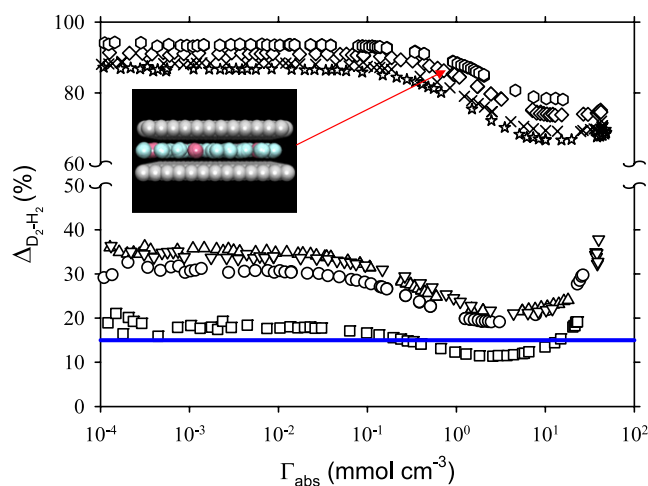
Figure 16. The differences between the pore density of D_2 and H_2 at 77 K for selected infinitely long atomistic slit-shaped carbon pore widths: 4.6 (squares), 5.6 (circles), 6.6 (up triangle), 3.6 (down triangle), 2.6 (stars), 2.55 (thin crosses), 2.45 (diamonds), 2.35 (hexagons) and 2.2 Å (bold crosses). Solid blue line denotes the difference between the density of deuterium and hydrogen measured for Carbotox charcoal at 77 K [1]. All theoretical results were obtained from simulation of D_2/H_2 equimolar mixture adsorption by the PI-GCMC method.

Figure 17. The differences between the pore density of D_2 and H_2 at 33 K for selected infinitely long atomistic slit-shaped carbon pore widths: 4.6 (squares), 5.6 (circles), 6.6 (up triangle), 3.6 (down triangle), 2.6 (stars), 2.55 (thin crosses), 2.45 (diamonds), 2.35 (hexagons) and 2.2 Å (bold crosses). Solid blue line denotes the difference between the density of deuterium and hydrogen measured for Carbotox charcoal at 33 K [1]. All theoretical results were obtained from simulation of D_2/H_2 equimolar mixture adsorption by the PI-GCMC method.

(figures 16 and 17). We predicted that the size of the slit-shaped carbon pores used for efficient sieving of hydrogen isotopes at 77 or 33 K should be lower than 2.6 Å (i.e. pore size that can accommodate exactly one layer of adsorbed hydrogen isotopes). For these small carbonaceous pores the ratio of the density of adsorbed D_2 and H_2 at 77 K is discontinuously increasing up to $\approx$50%. Further, for 33 K these small slit-shaped carbon pores are practically filled by pure deuterium molecules since quantum fluctuations of molecular hydrogen exceed the effective size of the slit-shaped carbon pore (i.e. H_2 molecules cannot be confined in carbon pores since their zero-point motion increases the kinetic energy up to high values). Our understanding of the D_2/H_2 mixture adsorption in carbonaceous porous materials can be used for designing an efficient D_2/H_2 molecular sieve operating at finite pressures.

4. Conclusions

Carbonaceous slit-shaped and square-shaped pores efficiently differentiate adsorbed hydrogen isotopes at 77 and 33 K. Extensive path integral Monte Carlo simulations revealed that the square-shaped carbon pores enhanced the selectivity of deuterium over hydrogen in comparison to equivalent slit-shaped carbon pores both at zero coverage and at finite pressures (i.e. quantum sieving of hydrogen isotopes is pore-topology-dependent). The enhancement in the D_2/H_2 equilibrium selectivity in square-shaped carbon pores results from a larger localization of hydrogen isotopes in comparison to equivalent slit-shaped carbon pores. The operating pressures for efficient quantum sieving of hydrogen isotopes are strongly dependent on both the topology as well as the size of the carbon pore. However, for both considered carbon pore topologies the highest D_2/H_2 separation factor is observed for zero coverage.

Depending on carbon pore size and topology we predicted monotonic decreasing and non-monotonic shape of the D_2/H_2 equilibrium selectivity at finite pressures. For both kinds of carbonaceous pores of molecular sizes we predicted high compression of hydrogen isotopes at 77 and 33 K (for example, the pore density of compressed hydrogen isotopes at 77 K and 0.25 MPa in square-shaped carbon pores of size 2.6 Å exceeds 60 mmol cm^{-3}; for comparison, the liquid density of *para*-H_2 at 30 K and 30 MPa is 42 mmol cm^{-3}). Finally, we explained why the ordinary carbonaceous materials are not efficient quantum sieves by direct comparison of simulation results with experimental data. Our simulation results can be directly used for the designing of an efficient D_2/H_2 molecular sieve operating at finite pressures.

References

[1] Van Dingenen W and Van Itterbeck A 1939 *Physics* **4** 389
[2] Hansen R S 1959 *J. Phys. Chem.* **63** 743
[3] Basmadjian D 1960 *Can. J. Chem.* **38** 141
[4] Basmadjian D 1960 *Can. J. Chem.* **38** 149
[5] Larin A V and Parbuzin V S 1992 *Mol. Phys.* **77** 869
[6] Polevoi A S, Khoroshilov A V and Yudin I P 1983 *Russ. J. Phys. Chem.* **57** 1063

[7] Polevoi A S and Yudin I P 1982 *Russ. J. Phys. Chem.* **56** 1982
[8] Polevoi A S and Yudin I P 1982 *Russ. J. Phys. Chem.* **56** 745
[9] Polevoi A S, Durneva A I and Azizov A S 1987 *Russ. J. Phys. Chem.* **61** 1987
[10] Levin M A, Gorbunov M B, Moskovskaya T A and Serpinskii V V 1986 *Russ. Chem. Bull.* **35** 2406
[11] Tanaka H, Kanoh H, Yudasaka M, Iijima S and Kaneko K 2005 *J. Am. Chem. Soc.* **127** 7511
[12] Tanaka H, Fan J, Kanoh H, Yudasaka M, Iijima S and Kaneko K 2005 *Mol. Simul.* **31** 465
[13] Beenakker J J M, Borman V D and Krylov S Y 1995 *Chem. Phys. Lett.* **232** 379
[14] Hoffmann J and Nielaba P 2003 *Phys. Rev.* E **67** 036115
[15] Wang Q, Challa S R, Sholl D S and Johnson J K 1999 *Phys. Rev. Lett.* **82** 956
[16] Challa S R, Sholl D S and Johnson J K 2001 *Phys. Rev.* B **63** 245419
[17] Challa S R, Sholl D and Johnson J K 2002 *J. Chem. Phys.* **116** 814
[18] Hathorn B, Sumpter B and Noid D 2001 *Phys. Rev.* A **64** 022903
[19] Garberoglio G, DeKlavon M M and Johnson J K 2006 *J. Phys. Chem.* B **110** 1733
[20] Feynman R P and Hibbs A 1965 *Quantum Mechanics and Path Integrals* (New York: McGraw-Hill)
[21] Feynman R P 1972 *Statistical Mechanics* (New York: Benjamin)
[22] Binder K and Heermann D W 2002 *Monte Carlo Simulation in Statistical Physics* (Berlin: Springer)
[23] Kowalczyk P, Gauden P A, Terzyk A P and Bhatia S K 2007 *Langmuir* **23** 3666
[24] Rabani E and Jortner J 2006 *J. Phys. Chem.* B **110** 18893
[25] Silvera I F and Goldman V 1978 *J. Chem. Phys.* **69** 4209
[26] Allen M P and Tildesley D J 1987 *Computer Simulation of Liquids* (Oxford: Clarendon)
[27] Steele W A 1974 *The Interaction of Gases with Solid Surfaces* (Oxford: Pergamon)
[28] Levesque D, Gicquel A, Darkrim F L and Kayiran S B 2002 *J. Phys.: Condens. Matter* **14** 9285
[29] Kowalczyk P, Tanaka H, Holyst R, Kaneko K, Ohmori T and Miyamoto J 2005 *J. Phys. Chem.* B **109** 17174
[30] Kowalczyk P, Holyst R, Terzyk A P and Gauden P A 2006 *Langmuir* **22** 1970
[31] Frenkel D and Smit B 1996 *Understanding Molecular Simulation From Algorithms to Applications* (London: Academic)
[32] Ceperley D M and Pollock E L 1986 *Phys. Rev. Lett.* **56** 351
[33] Pollock E L and Ceperley D M 1987 *Phys. Rev.* B **36** 8343
[34] Ceperley D M 1992 *Phys. Rev. Lett.* **69** 331
[35] Kowalczyk P, Brualla L, Zywocinski A and Bhatia S K 2007 *J. Phys. Chem.* C **111** 5250
[36] Nicholson D and Parsonage N G 1982 *Computer Simulation and the Statistical Mechanics of Adsorption* (London: Academic)
[37] Brualla L, Boronat J and Casulleras J 2002 *J. Low Temp. Phys.* **126** 1547
[38] McCarty R D, Hord J and Roder H M 1981 Selected properties of hydrogen *National Bureau of Standards Monograph* vol 168 (Washington, DC: US Government Printing Office)
[39] Nemirovsky D, Moreh R, Kaneko K, Ohba T and Mayers J 2003 *Surf. Sci.* **282** 526
[40] Nemirovsky D, Moreh R, Anderson K H and Mayers J 1999 *J. Phys.: Condens. Matter* **11** 6653